https://doi.org/10.18321/ectj1636

Efficient Photocatalytic Hydrogen Evolution via Cocatalyst Loaded Al-doped $SrTiO_3$

Zh. Kuspanov[1,2], A. Serik[1,2]*, A. Baratov[1,2], U. Abdikarimova[1,2], N. Idrissov[1,2], M. Bissenova[1,2,3], Ch. Daulbayev[1,2]

[1]Satbayev University, 22 Satbayev str., 050013, Almaty, Kazakhstan
[2]Institute of Nuclear Physics, 1 Ibragimov str., 050032 Almaty, Kazakhstan
[3]Institute of Physics and Technology, 11 Ibragimov str., 050032, Almaty, Kazakhstan

Article info

Received:
6 May 2024

Received in revised form:
27 June 2024

Accepted:
15 August 2024

Keywords
Photocatalytic water splitting;
$SrTiO_3$;
Cocatalysts;
H_2 evolution

Abstract

The growing reliance on fossil fuels is causing significant environmental issues, prompting the search for renewable energy sources. Hydrogen energy, which produces only water vapor, is a promising solution. This study focuses on developing an aluminum-doped $SrTiO_3$ photocatalyst with dual cocatalysts (Rh/Cr_2O_3 and CoOOH) for efficient photocatalytic water splitting. Using a simple chemical deposition method, high-purity and crystalline $SrTiO_3$ was synthesized and thoroughly characterized. The results show that the modified $SrTiO_3$ achieved significantly higher photocatalytic activity, with Rh/Cr_2O_3/$SrTiO_3$@Al/CoOOH producing 11.04 mmol g^{-1} h^{-1} of H_2 and 4.69 mmol g^{-1} h^{-1} of O_2. This work demonstrates the effectiveness of dual cocatalyst deposition and aluminum doping in enhancing photocatalytic performance by improving charge separation and reducing recombination.

1. Introduction

With population growth and technological advances, dependence on fossil energy sources is increasing, despite their limited reserves [1, 2]. The use of these fuels is accompanied by significant greenhouse gas emissions, leading to global environmental problems [3, 4]. Therefore, the scientific community is directing its efforts towards the development of renewable and clean energy sources [5, 6]. Hydrogen energy, of which water vapor is a by-product, is seen as one of the promising energy sources and requires innovative solutions to create cost-effective and environmentally friendly methods for mass production of hydrogen [7, 8, 9, 10]. One such method is the conversion of solar energy into green hydrogen through photocatalytic decomposition of water. In this context, the development of efficient photocatalysts becomes a key challenge. Oxide semiconductors such as $SrTiO_3$ with a 3.2 eV forbidden bandgap have proven to be efficient photocatalysts for water splitting under UV irradiation without applying an external voltage [11]. However, high-temperature synthesis of $SrTiO_3$ often produces defects that reduce the photocatalysis efficiency [12]. In particular, oxygen vacancies promote the reduction of Ti^{4+} to Ti^{3+}, which serve as recombination centers for the photogenerated electron-hole pairs [12]. Nevertheless, the ABO_3-type perovskite structure has considerable flexibility, which allows improving the photocatalytic activity by controlling and minimizing defects through cation substitution in the A- and B-sites [13]. Sources emphasize that efficient separation of photogenerated electron-hole pairs can significantly enhance photocatalytic activity [14]. Fine-tuning the physicochemical properties of the photocatalyst at the atomic level, e.g., through crystal facet engineering, contributes to charge

*Corresponding author.
E-mail address: aigerim.serik3508@gmail.com

selective separation and increased activity. Different crystal faces can direct electrons and holes to separate regions for reduction and oxidation, as observed in photocatalysts such as $BiVO_4$, BiOBr, and $SrTiO_3$ [15]. In addition, one approach to increase the efficiency of photocatalytic reactions is the use of dual co-catalysts deposited on the photocatalyst surface. Oxidation and reduction co-catalysts play an important role by helping to form active centers and facilitating the transfer of electrons and holes to different zones on the photocatalyst surface. Studies have shown that this promotes better separation of photogenerated pairs of electrons and holes, which increases the quantum yield of the reaction [16]. While the quantum efficiency of existing photocatalysts for water splitting is usually less than 10% at UV light, T. Takata and his colleagues were able to achieve an external quantum efficiency of up to 96% at wavelengths from 350 to 360 nm [17] using a modified photocatalyst based on aluminum-doped strontium titanate. This allows the hydrogen and oxygen release reactions to be carried out separately on different crystal faces of semiconductor particles, achieving maximum quantum efficiency for water splitting and eliminating charge recombination losses. Nevertheless, studies on efficient photocatalytic total water splitting using dual co-catalysts are currently insufficient, which opens the door for further research in this area.

Previous studies in our research [18, 19, 20] extensively explored the synthesis of $SrTiO_3$ nanoparticles using a simple and cost-effective chemical precipitation method followed by calcination. This approach enables the production of $SrTiO_3$ nanoparticles with relatively high purity while maintaining good photocatalytic activity. However, modifying pure $SrTiO_3$ by aluminum doping to introduce defect engineering, followed by the photodeposition of dual co-catalysts, could further enhance the photocatalytic performance of this material, particularly for water splitting and hydrogen production.

The aim of this work is to develop and study a photocatalyst based on aluminum-doped $SrTiO_3$ with the addition of double separately photodeposited co-catalysts for efficient water splitting. A simple chemical precipitation method was employed to synthesize $SrTiO_3$ of high purity and crystallinity. The structure, morphology and photocatalytic activity of the obtained materials were studied in detail. The results demonstrate a new and simple approach to the controlled synthesis and modification of $SrTiO_3$, providing high efficiency of photocatalytic water splitting.

2. Materials and methods

2.1 Materials

The main reagents and chemicals were purchased from Kazakhstan and the USA. These include TiO_2 (particle size less than 25 nm, purity 99.7%, Sigma-Aldrich, USA), $Sr(NO_3)_2$ (purity ≥ 98%, Sigma-Aldrich, USA), $(COOH)_2$-$2H_2O$ (purity greater than 98%, Sigma-Aldrich, USA), Al_2O_3 (particle size 50 nm, Sigma-Aldrich, USA), $SrCl_2$-$6H_2O$ (Laborpharma, Kazakhstan), $RhCl_3$-$6H_2O$ (Rh content 38–40%, Sigma-Aldrich, USA), $Co(NO_3)_3$-$6H_2O$ (purity ≥ 98%, Sigma-Aldrich, USA), and K_2CrO_4 (purity 99.5%, Laborpharma, Kazakhstan). All chemicals were of analytical grade and did not require additional purification. Double distilled water was used for synthesis and photocatalytic experiments.

2.2 Synthesis of $SrTiO_3$

$SrTiO_3$ powder was synthesized using a simple chemical precipitation method [18, 19, 20]. First, 0.12 M aqueous solution of $Sr(NO_3)_2$ was mixed with TiO_2 in distilled water at a Sr/Ti molar ratio of 1:1 and subjected to ultrasonic treatment for 30 minutes. A 0.4 M solution of $(COOH)_2$-$2H_2O$ was used as a reducing agent, which was added to the suspension dropwise under active stirring using a magnetic stirrer. The pH value of the suspension was then adjusted to 6–7 using 10% aqueous ammonia solution. After precipitation, the mixture was purified from excess ammonia by removing the surface liquid layer. The resulting precipitate was washed 5 times using centrifugation and dried at 60 °C for 16 hours. Finally, the product was calcined at 1100 °C in a muffle furnace in air.

2.3 Synthesis of $SrTiO_3$@Al

The alloying of $SrTiO_3$ powder with aluminum is carried out by the fluxing method developed by the team of Domen [17]. To synthesize $SrTiO_3$@Al, powders of 1.835 g $SrTiO_3$, 20.39 mg Al_2O_3, and 15.85 g $SrCl_2$ are mixed in an agate mortar for 15 min, or longer, until homogeneous. After thorough mixing, the mixture is calcined at 1150 °C for 10 h in a muffle furnace. The resulting powder is then ultrasonically treated to completely remove residual salt, after which it is washed 5 times with hot distilled water using centrifugation and dried for 20 h at 60 °C.

2.4 Photodeposition of $Rh/Cr_2O_3/SrTiO_3$@Al/CoOOH

Selective deposition of Rh/Cr_2O_3 and CoOOH double co-catalysts on the surface of $SrTiO_3$-based photocatalyst was carried out by photodeposition method. First, 0.1 g of $SrTiO_3$ or $SrTiO_3$@Al powder was mixed with 50 ml of distilled water and subjected to ultrasonic treatment for 30 minutes. The resulting suspension was placed in a photochemical reactor and irradiated with ultraviolet light from a 10 W mercury lamp under vigorous stirring. After magnetic stirring was started, 50 µl of $RhCl_3$-$6H_2O$ solution (2 mg/ml concentration) was added to the mixture and irradiation was continued for 10 minutes. Then 25 µl of K_2CrO_4 solution (2 mg(Cr)/ml) was added and irradiation was continued for another 5 minutes. Finally, 25 µl of $Co(NO_3)_2$ solution (2 mg(Co)/ml) was added and irradiated for 5 minutes. The resulting samples were washed several times and dried at 70 °C overnight.

2.5 Characterization

X-ray diffraction (XRD) on a Drone-8 instrument, scanning electron microscopy (SEM) with energy dispersive X-ray spectrometer (EDX), high-resolution transmission electron microscopy (HRTEM), and X-ray photoelectron spectroscopy (XPS) were used to characterize the synthesized samples. XRD measurements were performed over an angle range of 5–70° with a step size of 0.01° and an accuracy of ±0.015°. SEM and EDX were performed on a Zeiss Crossbeam 540 at an accelerating voltage of 5–20 kV. TEM was used to analyze the structure and distribution of co-catalysts on the photocatalyst surface using a JEM-2100 LaB6 at 80 kV. XPS was performed on a Microtech Multilab 3000 VG with Mg and Al sources, and the C1s level at 284.8 eV was used for calibration. Diffuse reflectance spectra (UV-Vis DRS) were recorded on a Perkin Elmer Lambda 35 spectrophotometer in the range of 200–800 nm.

2.6 Photocatalytic reaction

To determine the photocatalytic activity of the obtained samples, 25 mg of photocatalytic sample was suspended in 50 ml of distilled water and stirred for 30 min without the addition of sacrificial agents. The photocatalytic activity was evaluated by decomposition of water followed by release of hydrogen and oxygen. A Chromos-1000 chromatograph with 3 mm columns filled with NaX and PORAPAK Q was used to analyze the released gases. The photocatalytic water decomposition process was carried out in a photochemical reactor (Shanghai Leewen Scientific Instrument Co., Ltd., China), where a 10 W high-pressure mercury lamp with wavelength λ_{max} = 254 nm was used as a radiation source. The distance between a 50 ml quartz flask and the lamp was fixed at 10 cm.

3. Results and discussion

3.1. Characterization of obtained samples

SEM and TEM techniques were used to investigate the surface morphology of the samples. In the case of $SrTiO_3$ calcined at 1100 °C, the formation of agglomerated nanocubes with sizes ranging from 150 to 250 nm was observed (Fig. 1a). The calcination temperature proved to be a critical factor in determining the particle size. For example, calcination in the range of 750–900 °C forms smaller $SrTiO_3$ particles, but this process is accompanied by the appearance of $SrCO_3$ impurities [21]. Calcination at 1100 °C promotes the decomposition of carbonates, which ensures high phase purity and improves crystallinity, thereby enhancing the transfer efficiency of photogenerated charge carriers. Based on this, 1100 °C was selected as the optimum temperature for the synthesis of $SrTiO_3$ nanocubes. EDX analysis showed the presence of Sr, Ti and O in the structure without any extraneous impurities (Fig. 2). The doping of $SrTiO_3$ with aluminum nanoparticles resulted in the formation of truncated cubic particles with sizes ranging from 200 to 400 nm (Figs. 1b and 3a). Flux treatment followed by aging at 1150 °C promoted the broadening of {111} facets and the reduction of {100} [22], which improved the separation and transport of photogenerated charge carriers. This increases the photocatalytic activity of $SrTiO_3$ due to more efficient water reduction with hydrogen formation and oxidation with oxygen release. Figures 3b and 3c show $SrTiO_3$@Al samples after separate photodeposition of co-catalysts (Rh/Cr_2O_3 and CoOOH) on its surface. The images show that dark formations of 5–8 nm are concentrated on some faces, while less dispersed particles of 2–5 nm are localized on others. It is assumed that Rh/Cr_2O_3 nanoparticles are preferentially deposited on faces {100}, while CoOOH is distributed on faces {111} and {110}. These data are in agreement with previous studies that have examined in detail the growth of co-catalysts on the surface of $SrTiO_3$ [17, 22]. The unique distribution structure of the co-catalysts promotes efficient separation of photogenerated charges, which in turn facilitates the photocatalytic water splitting process.

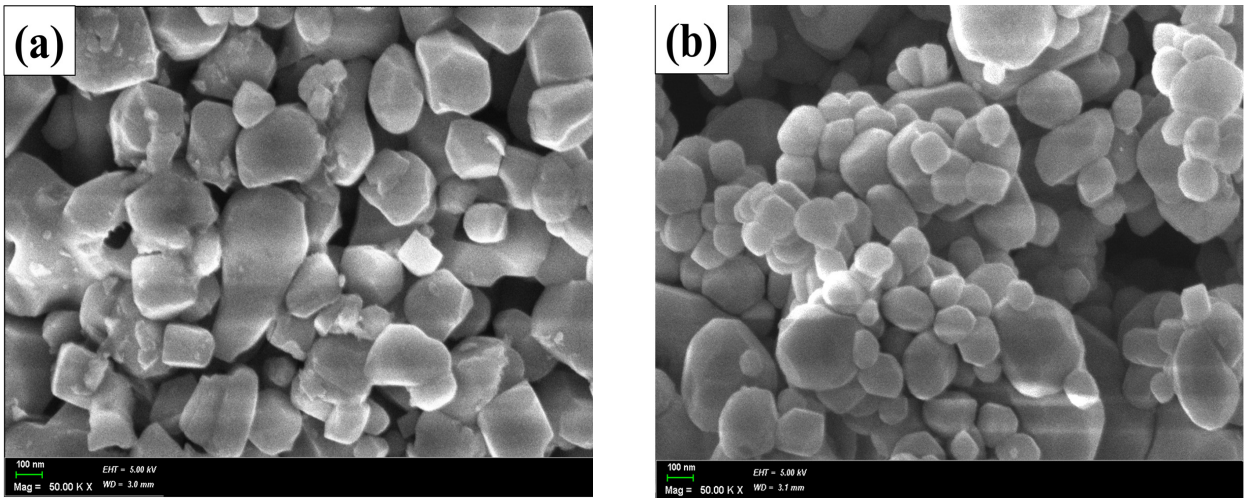

Fig. 1. SEM images of obtained (a) $SrTiO_3$ and (b) $SrTiO_3$@Al.

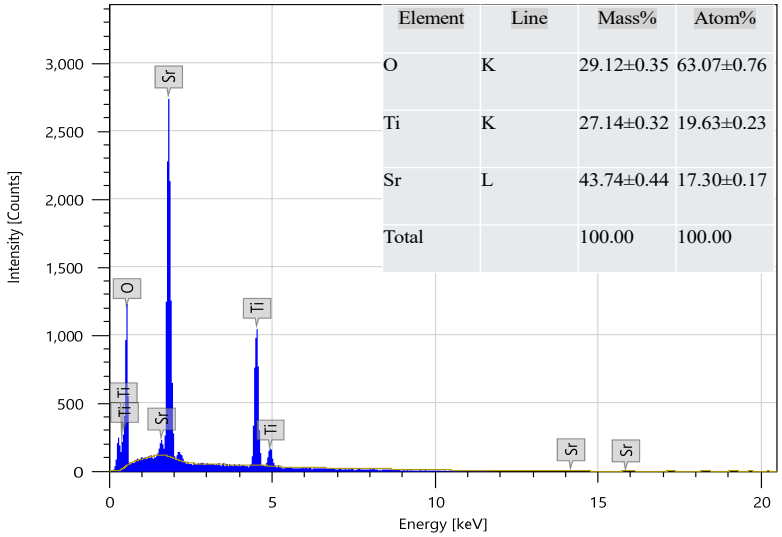

Element	Line	Mass%	Atom%
O	K	29.12±0.35	63.07±0.76
Ti	K	27.14±0.32	19.63±0.23
Sr	L	43.74±0.44	17.30±0.17
Total		100.00	100.00

Fig. 2. EDX spectrum of $SrTiO_3$ particles.

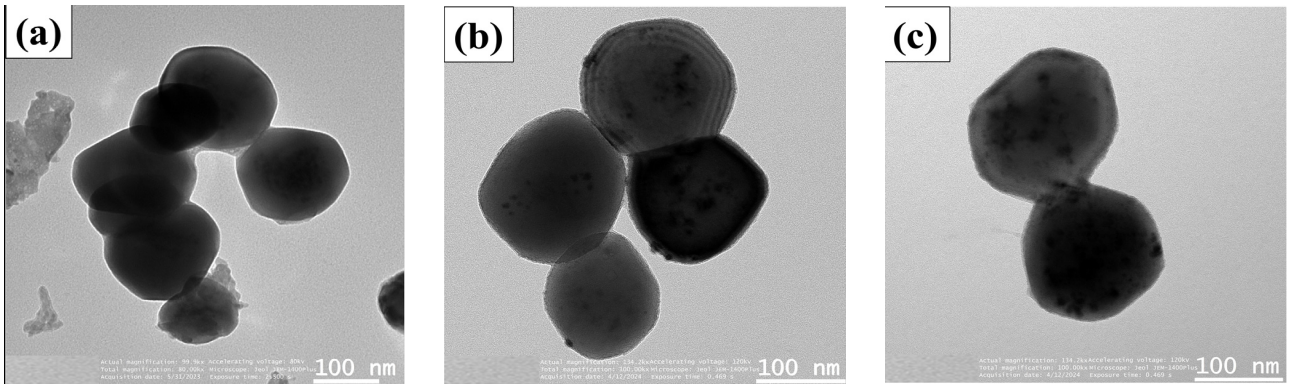

Fig. 3. TEM images of obtained (a) $SrTiO_3$@Al and (b,c) obtained cocatalyst loaded $SrTiO_3$@Al samples.

XRD spectra were studied for a detailed analysis of the crystal structure of the synthesized samples. Figure 4a shows the X-ray diffraction spectra for $SrTiO_3$, $SrTiO_3$@Al and $SrTiO_3$@Al samples with deposited co-catalysts. Diagnosis of the diffraction data shows that pure $SrTiO_3$ has a cubic perovskite structure [21]. The defined peaks for $SrTiO_3$ are recorded at 2θ angles of 32.40°, 40.50°, 46.50°, 58.50° and 68.50°, which correspond to the lattice planes of the cubic phase of $SrTiO_3$ ((110), (111), (200), (211) and (220) as reported in JCPDS Card #35-0734 [23]. Comparison of X-ray diffraction patterns for doped

and undoped $SrTiO_3$ shows a significant enhancement of peak intensities in the $SrTiO_3$@Al samples, indicating that aluminum doping improves the crystalline quality of $SrTiO_3$. Further, EDX mapping confirmed the presence of Ti, O, Sr and Al without any other impurities in the composition (Supplementary, Figs. S1, S2). At the same time, the presence of aluminum and co-catalysts does not change the crystal structure of $SrTiO_3$, since their peaks are not observed in the X-ray spectra. This is probably due to their low concentration, high dispersibility and low crystallinity [22].

XPS was used to analyze the changes in the chemical states and surface composition of $SrTiO_3$ samples before and after aluminum doping. The results are presented in Fig. 4 (b-d). In particular, the Ti 2p spectra (Fig. 4b) show two peaks: at 457.5 and 463.3 eV, corresponding to Ti $2p_{3/2}$ and Ti $2p_{1/2}$ states, respectively, indicating the presence of Ti^{4+} ions. The peak at 462.4 eV indicates the presence of Ti^{3+} ions in the $SrTiO_3$ sample [24]. After aluminum doping, Ti^{3+} ions completely disappear and the Ti 2p spectrum for $SrTiO_3$@Al contains only two peaks: 457.9 and 463.6 eV, which are associated exclusively with Ti^{4+} ions [24]. The energy level analysis for oxygen (O 1s) presented in Fig. 4 c shows two Gaussian peaks: one at 528.3 eV, corresponding to O^{2-} ions in the crystal lattice, and the other at 529.9 eV, indicating oxygen defects associated with oxygen vacancies. Aluminum doping leads to an increase in the defective oxygen ratio from 15.9 % to 54.2 %, which is consistent with data from other studies where the effect of aluminum on the photocatalytic properties of $SrTiO_3$ was investigated [25]. The optimal increase [12] in the number of oxygen defects upon aluminum doping contributes to the reduction of photogenerated carrier recombination and positively affects photocatalytic activity. The Sr 3d spectra show two peaks at 132.4 and 134.1 eV, corresponding to Sr $3d_{5/2}$ and Sr $3d_{3/2}$ states, respectively (Fig. 4d), confirming the presence of Sr^{2+} ions in $SrTiO_3$, which remains stable after aluminum doping. Overall, the XPS results for the synthesized samples are in agreement with other studies [24, 25].

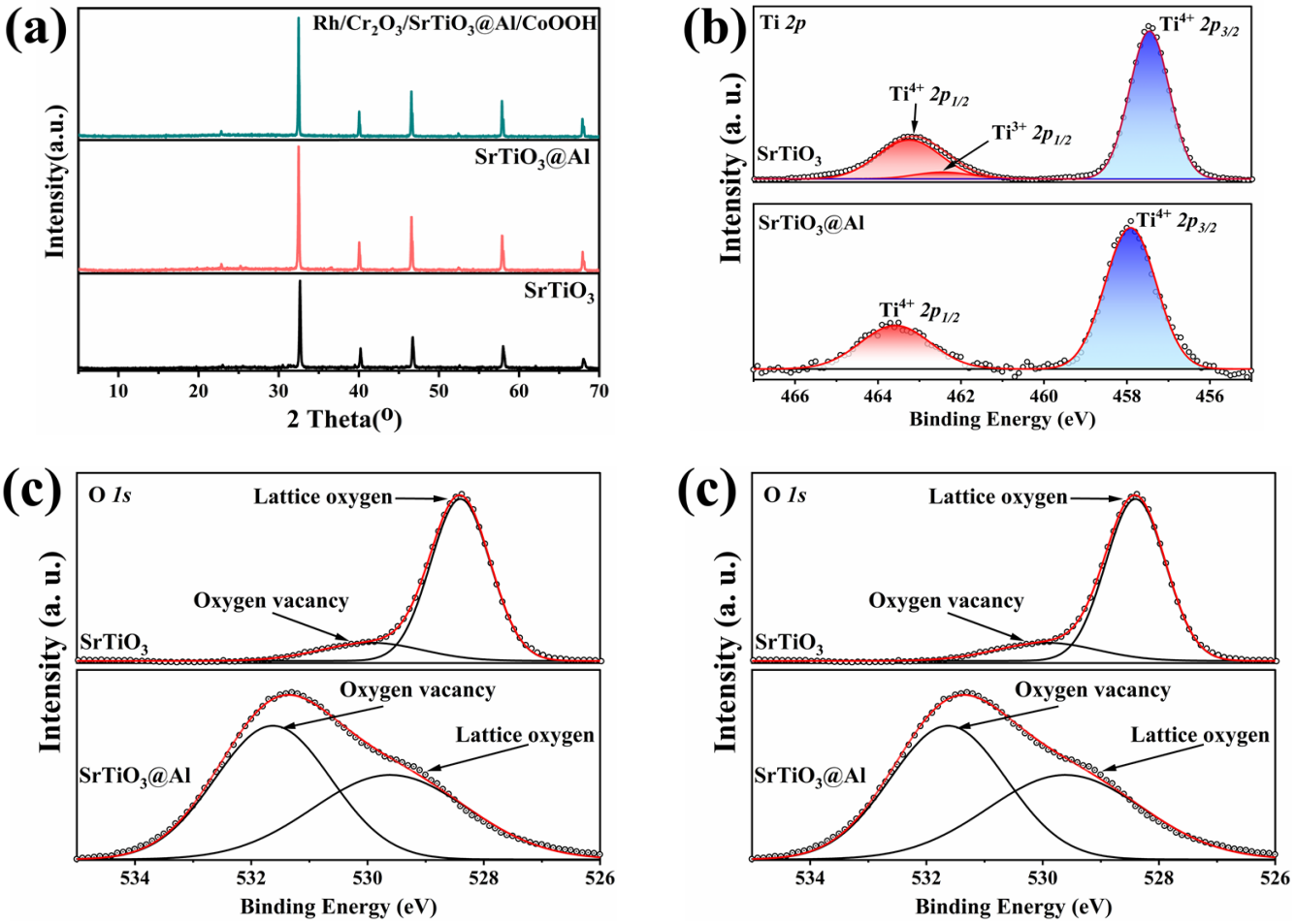

Fig. 4. (a) XRD patterns of prepared samples; XPS spectra of the $SrTiO_3$ and $SrTiO_3$@Al samples – (b) high-resolution Ti 2p, (c) O 1s and (d) Sr 3d.

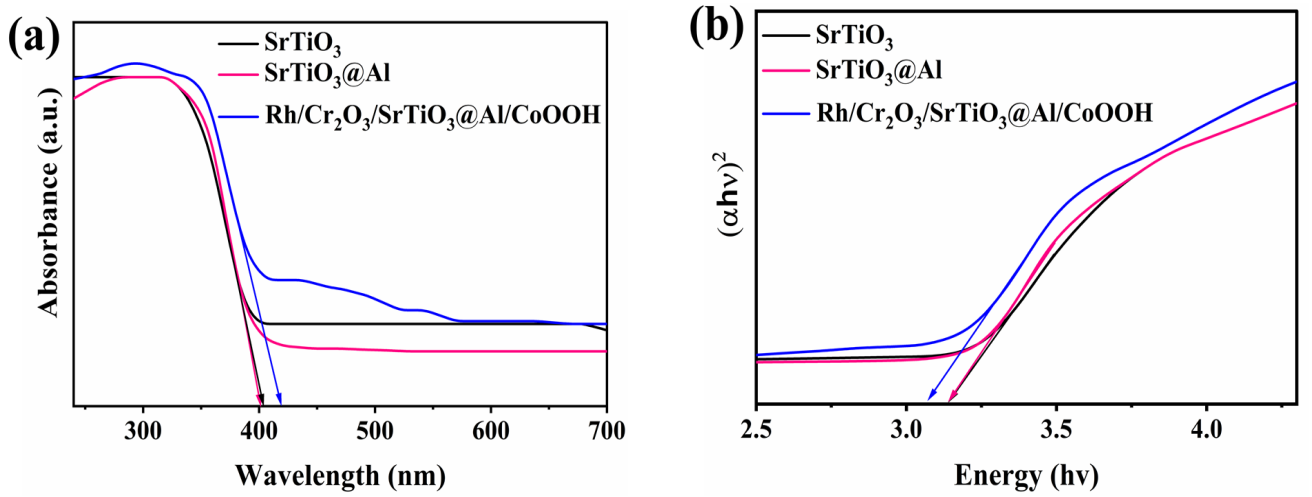

Fig. 5. (a) the UV-Vis DRS of the prepared samples and (b) the corresponding Tauc plots.

Figure 5 shows the UV-Vis absorption spectra for $SrTiO_3$, $SrTiO_3$@Al and $SrTiO_3$@Al with separately deposited co-catalysts in diffuse reflectance. The synthesized $SrTiO_3$ and $SrTiO_3$@Al samples exhibit light absorption up to a wavelength of 400 nm. At the same time, $SrTiO_3$@Al with co-catalysts shows a pronounced absorption peak around 425 nm shifted to the visible spectrum. To estimate the forbidden band width of photocatalysts, the dependence of $(\alpha h\nu)^2$ on photon energy was analyzed, where α is the absorption coefficient, h is Planck's constant, and ν is the photon frequency [26]. The forbidden band width was 3.13 eV for $SrTiO_3$@Al and 3.07 eV for $SrTiO_3$@Al with co-catalysts. These results show that aluminum doping has no significant effect on the light absorption properties compared to pure $SrTiO_3$ (Fig. 5b). Similar results have been obtained in other studies on the doping of $SrTiO_3$ with aluminum [12]. In particular, it is noted that doping with aluminum does not change the width of the forbidden band, but mainly reduces the undesirable defects Ti^{3+}, which serve as recombination centers for photogenerated charge carriers. For $SrTiO_3$@Al with co-catalysts, the bandgap width was slightly improved compared to $SrTiO_3$ and $SrTiO_3$@Al, indicating enhanced light absorption in the visible spectrum, especially in the violet and blue regions. However, the main advantage of co-catalysts is to reduce the recombination of photogenerated electrons and holes by improving their transport and separation [12].

3.2 Photocatalytic overall water splitting performance

Photocatalytic studies of total water splitting in the prepared samples were carried out and the results are presented in Fig. 6. The hydrogen and oxygen production rates per hour of the used photocatalysts are in the expected stoichiometric ratio for water splitting and are shown in Fig. 6. The bare $SrTiO_3$ and $SrTiO_3$@Al samples showed very low H_2 release rates of ~0.0036 and 0.0048 mmol h^{-1} g^{-1} due to less efficient reaction sites. After loading the co-catalysts, the photocatalytic total water splitting activity of the samples increased significantly (Fig. 6). In particular, the highest activity was achieved for the $Rh/Cr_2O_3/SrTiO_3$@Al/CoOOH sample with gas release rates of 11.04 and 4.69 mmol h^{-1} g^{-1} for H_2 and O_2, respectively, which significantly exceeded bare $SrTiO_3$ and $SrTiO_3$@Al by a factor of 3067 and 2300, respectively. It should be considered that the nonaluminum-doped $Rh/Cr_2O_3/SrTiO_3$/CoOOH photocatalyst showed a hydrogen evolution rate of 8.01 mmol h^{-1} g^{-1} under identical conditions. This confirms the results of previous studies, according to which the improved solar energy conversion

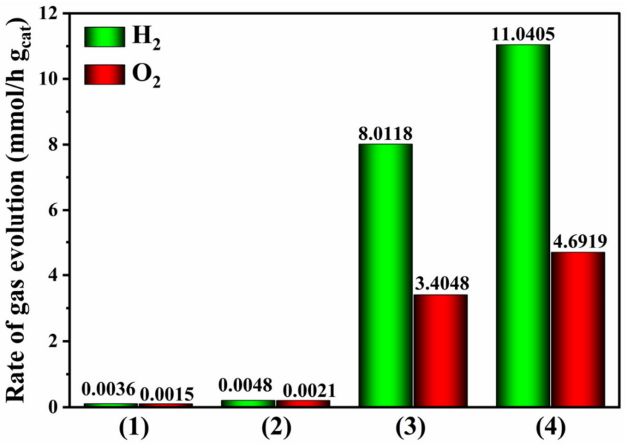

Fig. 6. Line graphs of photocatalytic H_2 and O_2 production performance of (1) bare $SrTiO_3$, (2) $SrTiO_3$@Al, (3) $Rh/Cr_2O_3/SrTiO_3$/CoOOH and (4) $Rh/Cr_2O_3/SrTiO_3$@Al/CoOOH under UV light irradiation.

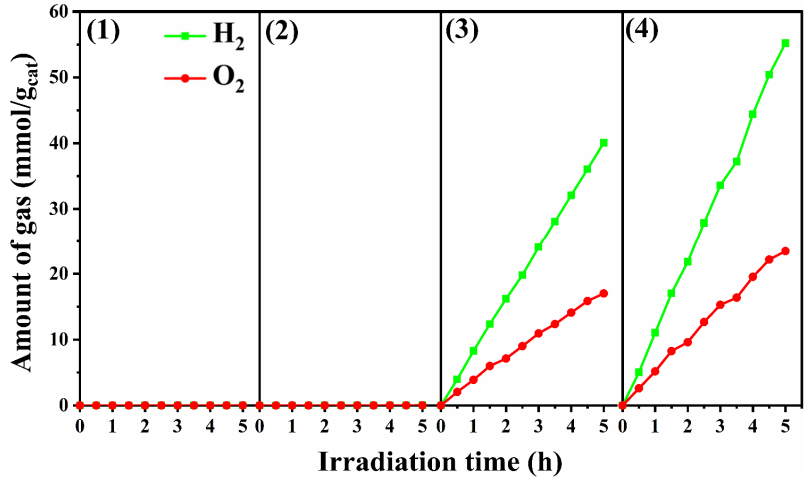

Fig. 7. Comparison of photocatalytic hydrogen production rates of (1) bare $SrTiO_3$, (2) $SrTiO_3$@Al, (3) Rh/Cr_2O_3/$SrTiO_3$/CoOOH and (4) Rh/Cr_2O_3/$SrTiO_3$@Al/CoOOH.

ability of Al:$SrTiO_3$ correlates with the Al content [17, 27]. As the reaction time increased, the rate of photocatalytic hydrogen formation increased linearly and reached 55.2 and 40.06 mmol g^{-1} after 5 h in the case of Rh/Cr_2O_3/$SrTiO_3$/CoOOH and Rh/Cr_2O_3/$SrTiO_3$@Al/CoOOH, respectively (Fig. 7). The linearity of the hydrogen production rate at different time steps is almost the same, indicating that the catalyst performance is relatively stable during this hydrogen production process. The high photocatalytic activity of the photocatalysts with loaded co-catalysts is due to the synergistic effect of separately photodeposited Rh/Cr_2O_3 and CoOOH (reducing and oxidizing) co-catalysts, which promotes efficient separation and transfer of photogenerated electrons and holes. Where the photodeposited Rh/Cr_2O_3 co-catalyst is responsible for the collection of electrons with subsequent hydrogen production, whereas CoOOH releases hydrogen due to the efficient collection of holes [17, 27]. In this way, charge recombination is minimized by sequential charge transfers between the photocatalyst and co-catalysts. In addition, the results of morphology and XPS analysis show that the use of flux method for aluminum doping resulted in the separation of reduction and oxidation zones by facet engineering, as well as the suppression of defects in the form of Ti^{3+}, which can serve as recombination centers.

Table shows comparisons with recent composite photocatalysts, which have relatively high results in photocatalytic water splitting. However, the photocatalyst synthesized in our laboratory significantly outperforms analogs in both H_2 and O_2 production. In addition, the above works used UV lamps with

Table. Comparison of the synthesized Cocat/STO@Al photocatalyst with the results of recent research

Year	Photocatalyst	Light source	Sacrificial agent	H_2 evolution rate (mmol h^{-1} g^{-1})	O_2 evolution rate (mmol h^{-1} g^{-1})	Ref.
2021	C–$SrTiO_3$/PAN/WS-FLG	120 W UV lamp, 254 nm	15 vol. % methanol	5.375	-	[9]
2022	Cr_2O_3@CoP/Al:STO	300 W Xe arc lamp	None	3.558	1.002	[28]
2023	Rh/Cr_2O_3/$SrTiO_3$@Al/CoOOH (hydrothermal method)	300W Xe-lamp	20 vol.% methanol	4.100	1.900	[27]
2024	Pd-loaded Al: $SrTiO_3$	300W Xe-lamp	20 vol.% methanol	1.430	-	[29]
2024	Rh/Cr_2O_3/$SrTiO_3$/CoOOH	10 W Mercury lamp	None	8.01	3.04	This work
2024	Rh/Cr_2O_3/$SrTiO_3$@Al/CoOOH	10 W Mercury lamp	None	11.04	4.69	This work

120 and 300 W power and used sacrificial agents to reduce recombination, which are undesirable and may cause difficulties in scaling [9].

4. Conclusion

This study successfully developed and investigated an aluminum-doped $SrTiO_3$ photocatalyst with dual, separately photo-deposited cocatalysts (Rh/Cr_2O_3 and CoOOH) for efficient water splitting. The results demonstrated a significant enhancement in photocatalytic activity, with the Rh/Cr_2O_3/$SrTiO_3$@Al/CoOOH sample achieving a hydrogen evolution rate of 11.04 mmol g^{-1} h^{-1}, which is substantially higher than non-modified samples. The enhanced performance is attributed to the synergistic effect of the cocatalysts, which effectively separate and transfer photogenerated charge carriers, minimizing recombination. Additionally, aluminum doping through a flux method improved crystal facet engineering and reduced defects like Ti^{3+}, further contributing to the catalyst's efficiency. These findings highlight the potential of aluminum-doped $SrTiO_3$ and dual cocatalysts in advancing photocatalytic water splitting technologies and offer a promising approach for future research in this field.

Acknowledgments

This research has been funded by the Science Committee of the Ministry of Science and Higher Education of the Republic of Kazakhstan (Grant No AP14869381).

References

[1]. G. Yergaziyeva, Z. Kuspanov, M. Mambetova, et al., *J. CO2 Util.* 80 (2024) 102682. DOI: 10.1016/j.jcou.2024.102682

[2]. J. Wang, W. Azam, *Geosci. Front.* 15 (2024) 101757. DOI: 10.1016/j.gsf.2023.101757

[3]. E. Dmitriyeva, I. Lebedev, E. Bondar, et al., *Eurasian Chem.-Technol. J.* 25 (2024) 211–217. DOI: 10.18321/ectj1543

[4]. G. Yergaziyeva, E. Kutelia, K. Dossumov, et al., *Eurasian Chem.-Technol. J.* 25 (2023) 21–32. DOI: 10.18321/ectj1492

[5]. E. Kutelia, K. Dossumov, M. Mambetova, et al., *AIP Conf. Proc.* 2803 (2023) 040015. DOI: 10.1063/5.0143475

[6]. V. Pavlenko, K. Temirkulova, A. Zakharov, et al., *Eurasian Chem.-Technol. J.* 25 (2024) 201–210. DOI: 10.18321/ectj1542

[7]. Q. Hassan, A.Z. Sameen, H.M. Salman, et al., *J. Energy Storage* 72 (2023) 108404. DOI: 10.1016/j.est.2023.108404

[8]. M. Yue, H. Lambert, E. Pahon, et al., *Renew. Sustain. Energy Rev.* 146 (2021) 111180. DOI: 10.1016/j.rser.2021.111180

[9]. E.V. Matus, I.Z. Ismagilov, E.S. Mikhaylova, Z.R. Ismagilov, *Eurasian Chem.-Technol. J.* 24 (2022) 69–91. DOI: 10.18321/ectj1320

[10]. I.Z. Ismagilov, E.V. Matus, V.V. Kuznetsov, H.C.L. Abbenhuis, *Eurasian Chem.-Technol. J.* 19 (2017) 3–16. DOI: 10.18321/ectj497

[11]. Z. Kuspanov, A. Umirzakov, A. Serik, *Int. J. Hydrogen Energy* 48 (2023) 38634–38654. DOI: 10.1016/j.ijhydene.2023.06.168

[12]. Z. Zhao, R. Goncalves, S. Barman, et al., *Energy Environ. Sci.* 12 (2019) 1385–1395. DOI: 10.1039/C9EE00310J

[13]. Y. Sakata, Y. Miyoshi, T. Maeda, et al., *Appl. Catal. A-Gen.* 521 (2016) 227–232. DOI: 10.1016/j.apcata.2015.12.013

[14]. Y. Liu, Y.-H. Li, X. Li, et al., *ACS Nano* 14 (2020) 14181–14189. DOI: 10.1021/acsnano.0c07089

[15]. Q. Shen, W. Kang, L. Ma, et al., *Chem. Eng. J.* 478 (2023) 147338. DOI: 10.1016/j.cej.2023.147338

[16]. M. Tayyab, Y. Liu, Z. Liu, et al., *Chem. Eng. J.* 455 (2023) 140601. DOI: 10.1016/j.cej.2022.140601

[17]. T. Takata, J. Jiang, Y. Sakata, et al., *Nature* 581 (2020) 411–414. DOI: 10.1038/s41586-020-2278-9

[18]. A.D. Kudaibergen, Z.B. Kuspanov, A.N. Issadykov, et al., *Eurasian Chem.-Technol. J.* 25 (2023) 139–146. DOI: 10.18321/ectj1516

[19]. M. Bissenova, A. Umirzakov, K. Mit, et al., *Molecules* 29 (2024) 1101. DOI: 10.3390/molecules29051101

[20]. A. Serik, Z. Kuspanov, M. Bissenova, N. Idrissov, et al., *J. Water Process Eng.* 66 (2024) 106052. DOI: 10.1016/j.jwpe.2024.106052

[21]. Y. Ma, Z. Wu, H. Wang, et al., *CrystEngComm* 21 (2019) 3982–3992. DOI: 10.1039/C9CE00495E

[22]. Y.-G. Lee, Y.-C. Cheng, Y.-T. Lin, et al., *J. Phys. Chem. C* 127 (2023) 9981–9991. DOI: 10.1021/acs.jpcc.3c00483

[23]. E. Rocha-Rangel, W.J. Pech-Rodríguez, J. López-Hernández, et al., *Arch. Metall. Mater.* 65 (2020) 621–626. DOI: 10.24425/amm.2020.132801

[24]. R. Li, T. Takata, B. Zhang, et al., *Angew. Chem. Int. Ed.* 62 (2023) e202313537. DOI: 10.1002/anie.202313537

[25]. H. Tan, Z. Zhao, W. Zhu, et al., *ACS Appl. Mater. Interfaces* 6 (2014) 19184–19190. DOI: 10.1021/am5051907

[26]. N. Ashurov, B. Oksengendler, S. Maksimov, et al., *Eurasian Chem.-Technol. J.* 24 (2022) 229–239. DOI: 10.18321/ectj1436

[27]. L. Tian, X. Guan, Y. Dong, et al., *Environ. Chem. Lett.* 21 (2023) 1257–1264. DOI: 10.1007/s10311-023-01580-8

[28]. S. Zong, L. Tian, X. Guan, et al., *J. Colloid Interface Sci.* 606 (2022) 491–499. DOI: 10.1016/j.jcis.2021.08.049

[29]. J. Jiang, Y. Zhou, J. Zhang, et al., *Int. J. Hydrogen Energy* 82 (2024) 646–654. DOI: 10.1016/j.ijhydene.2024.07.441